Proceedings of ASME Turbo Expo 2011
GT2011
June 6-10, 2011, Vancouver, British Columbia, Canada

GT2011-46433

POTENTIAL FLOW FIELD GENERATED BY DOWNSTREAM MOVING BARS AND PROPAGATED ON A TURBINE BLADE AT LOW REYNOLDS NUMBER

Véronique Penin*
Pascale Kulisa
François Bario

Laboratoire de Mécanique des Fluides et d'Acoustique
UMR 5509
Ecole Centrale de Lyon
Université de Lyon UCB Lyon 1
INSA Lyon
36, avenue Guy de Collongue 69134 Écully Cedex
France
Email: veronique.penin@ec-lyon.fr
pascale.kulisa@ec-lyon.fr
francois.bario@ec-lyon.fr

ABSTRACT

During the last few decades, the size and weight of turbomachinery have been continuously reduced. However, by decreasing the distance between rows, rotor-stator interaction is strengthened. Two interactions now have the same magnitude: wake interaction and potential effect. Studying this effect is essential to understand rotor-stator interactions. Indeed, this phenomenon influences the whole flow, including the boundary layer of the upstream and downstream blades, ergo the stability of the flow and the efficiency of the machine.

A large scale turbine cascade followed by a specially designed rotating cylinder system is used.

Synchronised velocity LDA measurements on the vane profile show the flow and boundary layer behavior due to the moving bars.

To help the general understanding and to corroborate our experimental results, numerical investigations are carried out with an unsteady three dimensional Navier-Stokes code. Moreover, the numerical study informs about the potential disturbance to the whole flow of the cascade.

NOMENCLATURE

C	chord
C_f	friction coefficient $C_f = \frac{\tau_{wall}}{\frac{1}{2}\rho V_{ext}^2}$
C_p	pressure coefficient
C_x	axial chord
d	downstream cylinder diameter
f_r	reduced frequency
g	cascade pitch
H_{12}	shape factor
k	turbulent kinetic energy
l	characteristic integral length scale
LE / TE	leading edge / trailing edge
P	static pressure
P_t	stagnation pressure
PS/SS	Pressure Side / Suction Side
Re_c	chord Reynolds number $Re_c = \frac{CV_{out}}{\nu}$
T_0	period

*Address all correspondence to this author.

T_u	turbulence intensity
U	rotation velocity
V_{abs}	absolute velocity
V_{ext}	velocity out of the boundary layer
V_{in}	inlet velocity
V_{out}	outlet velocity
V_p	potential velocity : $V_p = \sqrt{\frac{2\times(P_{t_{in}}-P)}{\rho}}$
y	normal to the wall in the tangential direction
α	absolute flow angle
δ	boundary layer thickness $V(\delta) = 0.995V_{ext}$
δ_1	displacement thickness
δ_2	momentum thickness
ν	kinematic viscosity
ϕ	flow factor : $\phi = \frac{V_{in}}{U_{bar}}$
ρ	density
τ_{wall}	wall shear stress

INTRODUCTION

Rotor-stator interactions are unsteady 3D phenomena, row geometry and row motion create two kinds of interactions. The wake effect is a well-known viscous one. It only affects the downstream flow. On the contrary, the potential pertubation due to the presence of a body propagates in the whole flow, and decays exponentially to become insignifiant one chord length further in both directions. That is why it has generally been neglected.

Nowadays, the size and weight of turbomachinery are reduced, strengthening rotor-stator interaction. As the row gap is smaller, the potential effect has to be considered ([1], [2]). Just a few studies focus on this effect in turbines ([3], [4]) or in compressors [5]. In these cases, the potential field and the wakes induce the same order of perturbation magnitude [6]. These phenomena influence the whole flow and specially the blade boundary layer. Having a better understanding of rotor-stator interactions on the downstream and upstream blade boundary layer will probably permit an increase in engine performance.

Parker *et al.* ([3], [7], [8]) investigate rotor-stator interaction. They show, thanks to different relative fixed positions of two following rows, that the mean effect of the downstream row on upstream is a blockage effect. In fact, the downstream blades disturb the circumferential acceleration which appears if there is no downstream row or with a faster turning downstream row. This blockage gives birth to azimutal velocity fluctuations, depending on the relative position of the downstream row. So Parker et al. ([6], [9]) conclude that the potential field generated by a downstream row is similar to a quasi period wave with a downstream row velocity frequency.

Opoka and his co-workers [4] experimentally study the potential field in a large-scale low pressure turbine cascade. This study shows that bars downstream of the cascade influence the blade boundary layer. With the blade geometry used, the boundary layer transition onset appears further upstream than in the steady case at low turbulence intensity, whereas at high turbulence intensity, the separation of the boundary layer is periodically suppressed.

In our study, we choose a very large scale turbine cascade, with LP turbine Reynolds number (Re_c = 1.8.10^5). This configuration enables us to have a thick boundary layer, so the boundary layer description will be easier to obtain and more detailed. With 0.2 vane axial chords between the rows, we ensure there is a sufficiently strong potential field, generated by moving downstream rods, to influence the upstream cascade, as found by Deslot [10]. She also demonstrated by a steady numerical simulation that the boundary layer of our blade, without downstream rows, does not separate.

Flaps are added downstream of the rods to facilitate the outlet flow periodicity setting. The flaps are aligned with the blade wake. We will see their effects on the flow.

EXPERIMENTAL FACILITIES

This research was performed on a low speed large scale cascade composed of five blades (Fig.1 and Tab.1). The untwisted blades are typically an inlet guide vane with a zero inlet angle. They are followed by moving bars and flaps. The configuration can be compared to a one-and-a-half stage, with the same pitch for the three rows. The rod diameter adopted corresponds to the size of the leading edge of the downstream rotor blade in a real turbine. Four positions of the rod, equally distributed on a pitch g (or a rod passing period T_0), are focused on for this study (Fig.2), spatially, noted REF, $T_0/4$, $2T_0/4$ and $3T_0/4$, corresponding to instants $t = 0$, $t = T_0/4$,$t = 2T_0/4$ and $t = 3T_0/4$.

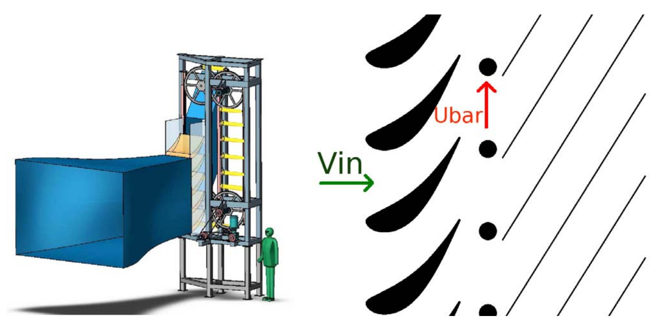

FIGURE 1. Cascade

Pressure measurements

Upstream of the cascade, a Pitot probe measures the inlet velocity V_{in}. The middle blade of the cascade is fitted with 37

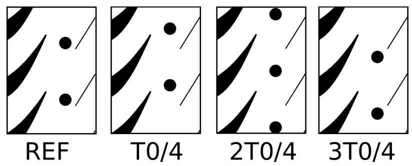

FIGURE 2. Studied positions of the rods

Blade chord C	0.704m
Axial blade chord C_x	0.514m
Cylinder diameter d	0.1m
Flap length L_f	1.5m
Vane-rod axial spacing	0.1m
Rod-flap axial spacing	0.03 m
Pitch g	0.457m
Inlet velocity V_{in}	1.72 $m.s^{-1}$
Cylinder velocity U_{bar}	2 $m.s^{-1}$
Chord Reynolds number Re_c	1.8×10^5

TABLE 1. Geometry and aerodynamic parameters

pressure taps (21 on the suction side). The potential velocity V_p is based on the pressure measured on the blade surface and total pressure measured with a Pitot probe half an axial chord upstream of the blade. Two DP103 validyne differential pressure sensors (3mmCE range) with a CD15 Sine Wave Carrier Demodulator are used to obtain V_{in} and V_p. The data are recorded with a 31 point ensemble average of 1500 samples at a 3000 Hz rate. Thus we obtain the experimental V_{in}.This velocity is used to make the experimental data dimensionless. An optical system detects the rod position, and the Labview software program gives us the V_p phase average, with respect to the moving rods period. The raw data are recorded according to the rod position. Then a classical phase average is applied. We choose to use 200 periods of this phenomenon (200 bars pass in front of the equipped blade), resulting from an ensemble average of 1500 samples at an acquisition frequency of 3000 Hz.

LDA instrumentation

To explore the boundary layer on the blade, a two dimensional LDA system is used. Two beams (one green and one blue, 514.5 nm & 488 nm wavelength respectively) are generated by the laser, and cross a Bragg cell. Four laser beams are obtained and their intersection gives the measurement volume ($0.0658 \times 0.0655 \times 0.731\,\mathrm{mm}^3$). So we have two orthogonal velocity components, which are acquired simultaneously. Then, we obtain two coincident velocity components synchronized with the rod frequency.

At each spatial position, 500,000 pieces of information are recorded to assure a good phase average calculation (enough passing bars and enough particles during a giving period). Each period is divided into 140 time intervals.

COMPUTATIONAL ANALYSIS

Fluid and turbulence models

The physical model of the flow is based on three-dimensional compressible Navier-Stokes equations with a two dimensional equation Smith k-l model [11]. Deslot detailed the numerical process in [12].

This model was previously evaluated for different turbomachinery configurations [13] and is suitable for such applications.

The numerical code used for this study is the elsA solver developed by Onera [14]. This code, dedicated to research and industrial applications, solves the compressible three-dimensional Navier-Stokes equations with a finite volume approach on structured multi-block grids. The unsteady terms are treated by backward Euler integration with implicit schemes solved by LU relaxation methods. The spatial terms are discretized in a relative moving frame, through a centered Jameson scheme [15]. Second and fourth order dissipative terms are added to ensure numerical stability. The viscous terms are discretized by a 2nd order centered scheme.

For the unsteady application, the time step is consistent with the size of the space cell.

Because of the very low speed configuration studied here, a preconditioning method ([16], [17]) is used. This technique, initially developed by Chorin [18], is not only used to accelerate convergence, but precision is also improved by conditioning the dissipation terms, initially of the order of unity, to the order of the Mach number [19]. This consists in multiplying the temporal derivative of the Navier-Stokes equation by a preconditioning matrix. The Weiss-Smith method, known to limit the vorticity production generated by the preconditioning method, is adopted. The numerical technique is explained in detail in [10].

To know the nature of the boundary layer, the Arnal Habibballah Delcourt transition criterion is adopted [20]. This non local criterion permits the natural transition, the transition due to adverse pressure gradients or boundary layer separation to be detected.

Mesh strategy

The Numeca turbomachinery grid generator Autogrid is employed for meshing. The two dimensional blade profile is piled up in the hub-to-casing direction to obtain the three dimensional mesh. A multi-domain approach is used with O-6H topology for each row (Fig.3, only 1/25 nodes are represented). An O-grid is defined around each profile to allow a precise description of the near-wall and leading edge regions. H-O-H topology associated with two additional azimutal H domains are necessary to define the geometry correctly without generating low orthogonality cells. The H inlet extension is two blade axial chords upstream of the blade leading edge while the H outlet extension is half a flap length downstream of the flap. The construction of the mesh satisfies the constraint of a first cell wall distance for the airfoil such that its height is equal to or lower than unity, considering the skin friction coefficient measured previously by Bario([21]). The mesh is composed of roughly 500,000 points.

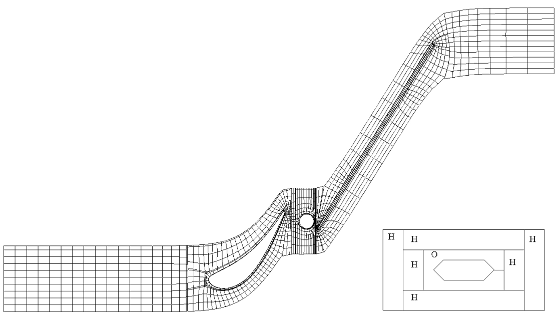

FIGURE 3. Mesh and O-6H topology

Boundary conditions

Because the flow is subsonic, stagnation pressure and temperature and flow angles are prescribed at the inlet of the domain. The static pressure is given in the outlet section. Inlet and outlet boundary conditions are constant in the vertical direction. Periodic conditions are applied in the spanwise direction. A large number of blades is considered in the calculation, thus the row radius is very large to reproduce the experimental linear cascade. For turbulence resolution, the turbulent kinetic energy is deduced using Bradshaw's relation k_∞. A 2.5% freestream turbulence intensity (including the fluctuations of the two components of the velocity) is adopted and the characteristic l integral length scale is fixed at 1% of the blade pitch. The periodicity of the different fields is ensured on the azimutal boundaries of the computational domain. Adiabatic conditions are prescribed on the solid boundaries, and adiabatic non-slip conditions on the side-walls. All the quantities are transmitted through the interface between the blade, the cylinder and the flap meshes. Since no tip clearance flow is simulated, both hub and casing rotate with the rod.

Convergence

Convergence is observed through time-averaged mass flow for unsteady simulations. The difference between the upstream and the downstream mass flow must be less than 1%. Moreover the decrease of the residual is verified.

RESULTS

Inlet results

Fig.4 displays a comparison between the experimental velocity and the numerical one on the cascade pitch at $0.29C_x$ upstream of the cascade. The experimental data are obtained with the LDA system. Resultats are in a good agreement.

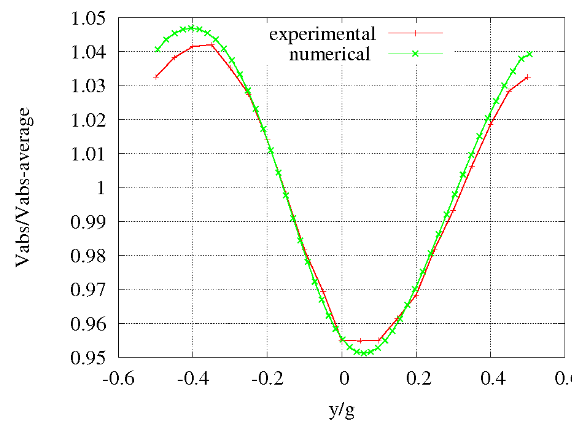

FIGURE 4. Experimental and numerical velocity upstream of the cascade

Unsteady case - moving rods

Four rod positions are selected for presentation (Fig.2). The flow factor ϕ is 0.86 for the experimental and numerical configurations.

Numerical results

Pressure coefficient Fig.5 shows the evolution of the pressure coefficient C_p (eq.1) over a period (the high pressure zone is blue and low pressure zone is red). The position of maximum velocity on the suction side is approximately at $0.4C_x$ after the leading edge (LE).

$$C_p = \frac{P_{t_{in}} - P}{P_{t_{in}} - P_{out}} \tag{1}$$

First, the C_p field varies a lot over the period, from the inlet to the outlet of the configuration. This reveals a global effect due to the unsteady blockage effect of the rod.

The strongest variations take place close to the blade suction side, in the inter-row passages, around the rod and in the inter-flap channel.

Behind the rod, a low pressure zone is created. This area takes on various shapes. It is small at $3T_0/4$, and more extensive at $T_0/4$. A low pressure bubble, detached from the rod's trailing edge (TE) at $T_0/4$, is convected downstream at $T_0/4$ and $2T_0/4$ to become just perceptible at the reference position REF. It results from the influence of the blade wake (Fig.7) and the flap (Fig.6).

A local effect, due to the streamline deviation generated by the moving rods, is noticeable. Indeed, the size and shape of the low pressure zone in the inter-blade channel fluctuate over the moving rod period. The largest low pressure zone is detected at $3T_0/4$, and goes upstream more than at the $T_0/4$ position.

Therefore this configuration successfully throws light on the potential effect. Unfortunately, the moving rod also complexifies the whole flow, like the blade wake propagation, and enhances the blockage effect due to the rod.

Absolute velocity and entropy Fig.6 displays velocity fields, whereas entropy fields are presented in Fig.7. Two extreme cases are recognized : when the rod is aligned with the blade wake ($3T_0/4$), and when the rod is in the middle of the inter-blade channel flow at $T_0/4$.

At $3T_0/4$ (Fig.6), the rod and blade wakes are aligned and merge into one larger wake impacting the flap (Fig.7). The acceleration zone is wider at the bottom part of the rod, and spreads to the inter-flap channel, leading to an asymmetrical wake. At $2T_0/4$, the rod cuts across the blade wake. The entropy accumulation on the rod top comes from the SS wake; whereas the PS wake part has not reached the rod bottom yet (it does so at $3T_0/4$ in Fig.7).

To explain the sinusoidal shape of the velocity or entropy regions in the inter-flap channel, and also the C_p bubble, the periodic variation of the flow around the rod must be analyzed. At $T_0/4$, the rod wake is clearly separated from the blade wake, even if, it is beginning to disturb it. Then the rod cuts across the blade wake. At the reference position REF, the flow around the rod undergoes a strong acceleration because of the very close flap. This acceleration is due to the flap blockage effect present at $3T_0/4$. At the reference position REF (in Fig.7), the strong acceleration begins to split the rod wake. This phenomenom still exists at $T_0/4$, where the rod is aligned in the middle of the inter-blade channel. Then, in Fig.5 at $T_0/4$, the high C_p zone breaks away from the rod. This is a consequence of the strong acceleration due to the flap blockage effect at $3T_0/4$. Hence this periodic effect leads to the velocity (and entropy) sinusoidal shape and to a C_p bubble convecting along the inter-flap channel.

The velocity around the blade is modulated by the moving

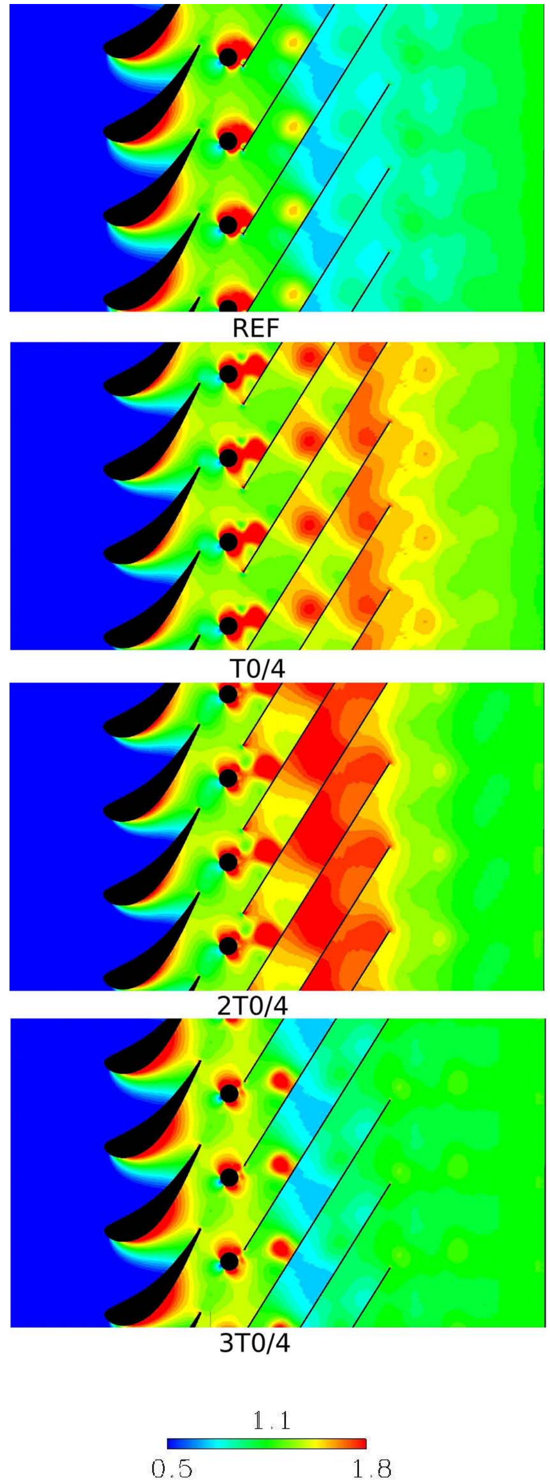

FIGURE 5. Pressure coefficient C_p

bars (Fig.6). The acceleration on the SS is more or less pronounced. At $3T_0/4$, another acceleration area appears near the TE because of the reduction of the blade-rod channel. Conversely, for the reference position REF, this zone undergoes deceleration. Thus the velocity outside the boundary layer V_{ext} is unsteady.

These interactions between blade wake, potential field around the rod and the flap induce a complex flow. The zone close to the suction side is of critical importance in our investigation. Hence, in this region, C_p varies greatly according to the rod's position, which could modify the stability of the blade boundary layer, hence the machine's efficiency.

Velocity profile Fig.8 presents the numerical and experimental velocity distributions on the blade. The experimental data come from the pressure measurements. Very good agreement is noticed. The vertical lines signal the extent of the local velocity fluctuation during a rod passing period T_0 (minimum and maximum velocities).

From 0 to 0.4 C_x, at the SS, the flow accelerates. Then, the velocity decreases slowly up to the TE, where strong variations of the velocity occur (Fig.6). At the PS, the flow velocity increases continously from the LE to the TE. This surface pressure evolution is consistent with the velocity distribution of a low pressure turbine blade. As no ”plateau” is distinguishable between the velocity peak and the trailing edge in any instantaneous curve, one can assume there is no separation bubble on the suction side.

The largest local fluctuations take place on the rear part of the SS, which is consistent with the results of the previous section.

Friction coefficient The friction coefficient C_f (Fig.9) brings to light the state of the boundary layer. As C_f decreases up to $0.85C_x$, the boundary layer on the SS is laminar. It remains laminar up to the TE at $2T_0/4$ and $3T_0/4$. At the reference position REF, this friction coefficient increases, then decreases again. That means that the boundary layer undergoes a transition up to $0.87C_x$. This unsteady behavior of the friction coefficient therefore reveals the unsteady nature of the boundary layer during a moving rod period.

Experimental results We focus our presentation of experimental results on the flow close to the trailing edge.

The measurements are acquired as mentioned in the LDA instrumentation section at $0.97C_x$ on the SS, and at $0.95C_x$ on the PS. The data are presented for four different instants (or rod locations). LDA measurements were made down to 0.12mm from the wall on the SS and to 0.35mm on the PS.

Fig.10 and Fig.11 illustrate the velocity variation during a period T_0, for different distances to the wall $y/\delta_{(t=0)}$ (where

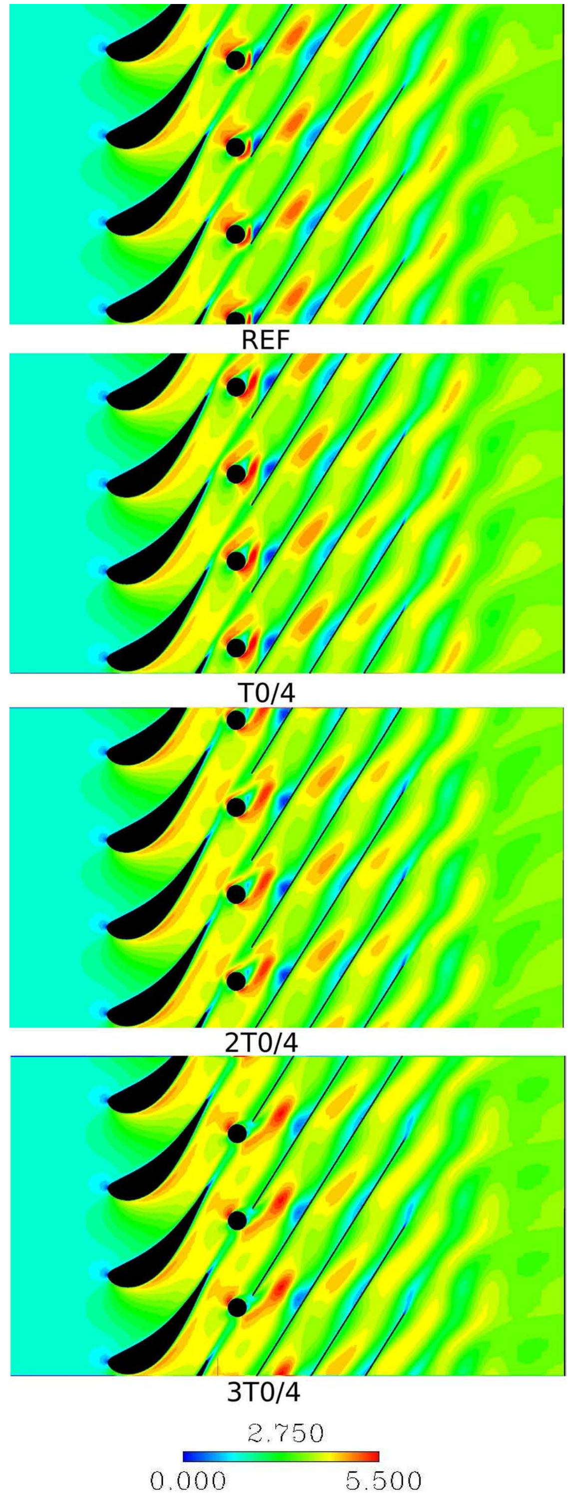

FIGURE 6. Absolute velocity V_{abs}

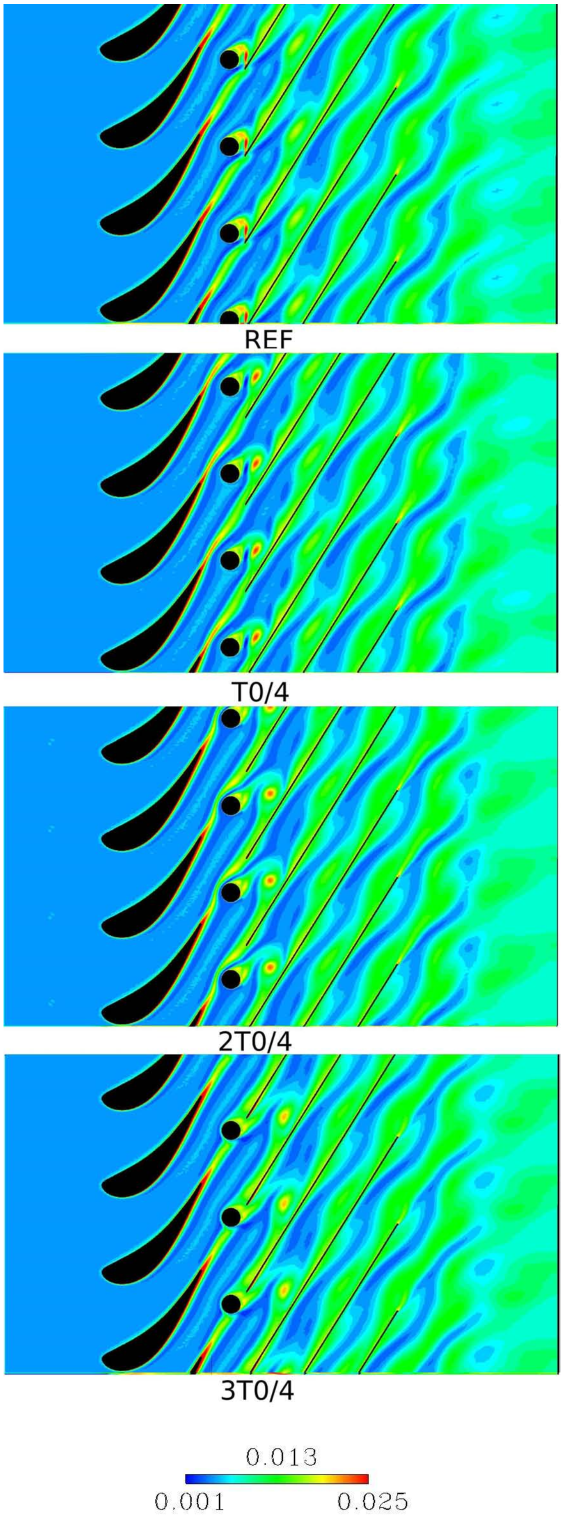

FIGURE 7. Entropy

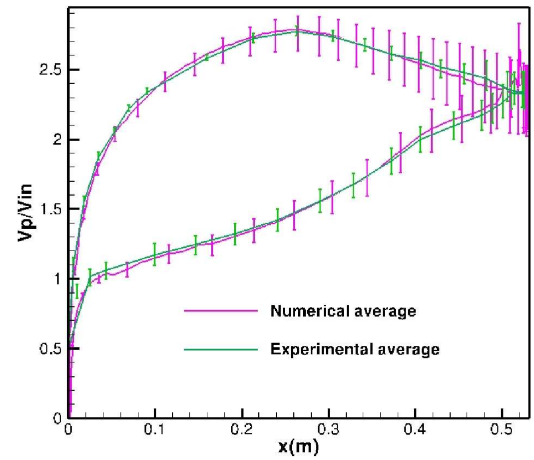

FIGURE 8. Experimental and numerical velocity profile on the blade

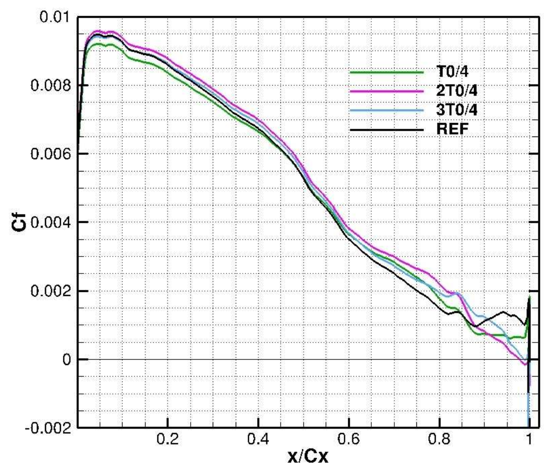

FIGURE 9. Numerical friction coefficient on the suction side

$\delta_{(t=0)}$ is the boundary layer thickness at the time t=0 (rod location REF), see Tab.2 and Tab.3) on the suction side and on the pressure side respectively.

On the suction side (Fig.10), outside the boundary layer ($y/\delta_{(t=0)} > 1$), the absolute velocity V_{abs} (ie V_{ext} for these $y/\delta_{(t=0)}$) is time dependent. The fluctuations (roughly 20% of fluctuation) are consistent with the numerical results.

On the pressure side (Fig.11), the variation of the absolute velocity V_{abs} is less pronounced (only 1%). The numerical results are overestimated. The potential effect of the rods mainly affects the suction side of the blade.

The boundary layer is laminar on the pressure side (Fig.12) and does not show much evolution over time. This is corraborated by the velocity fluctuation (turbulence level) measured within the boundary layer (no change compared with the external value, figure not shown), and by the shape factor (Tab.2). The thickness of the boundary layer is about 0.005m.

On the contrary, on the suction side, there are strong changes in both dimensional and dimensionless representations of the boundary layer (Fig.13 and Fig.14). The turbulence intensity (the sum of the fluctuations of the two measured components divided by the velocity outside the boundary layer $V_{ext}(t)$) is shown in Fig.15. There is an increase of the turbulence intensity in the boundary layer for all times, showing that the transition has begun. Outside the boundary layer, the turbulence level is $T_u = 2.5\%$, which is a phase locked value, only due to "classical" turbulence. The "turbulence intensity" including the periodic fluctuation of the flow due to the rod motion is 7.2%, but it has no real significance for the boundary layer behavior. The shape factor H_{12} varies from 1.7 to 2.6 (Tab.3), the thickness of the boundary layer is about 0.01m. The shape factor and the distribution of the turbulence intensity in the boundary layer show that the flow is still transitional for all the selected times. At $t = T_0/4$ and $t = 2T_0/4$, the transition is delayed compared to $t = 0$ and $t = 3T_0/4$. The numerical results obtained for the friction coefficient C_f show the same trend : for $t = 0$ (REF), there is an increase of the friction coefficient, indicating a deeper transition compared to other times.

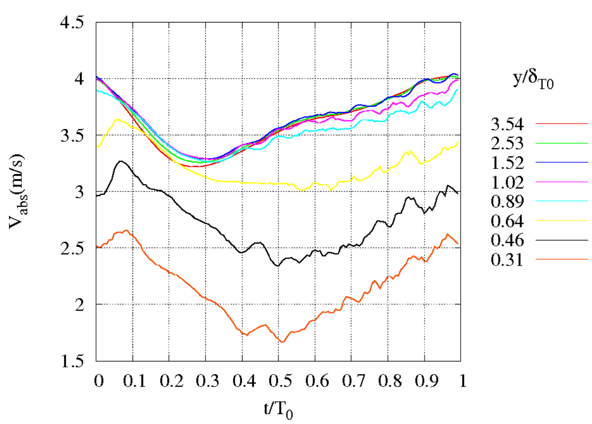

FIGURE 10. Velocity distribution on the suction side during a moving bar period

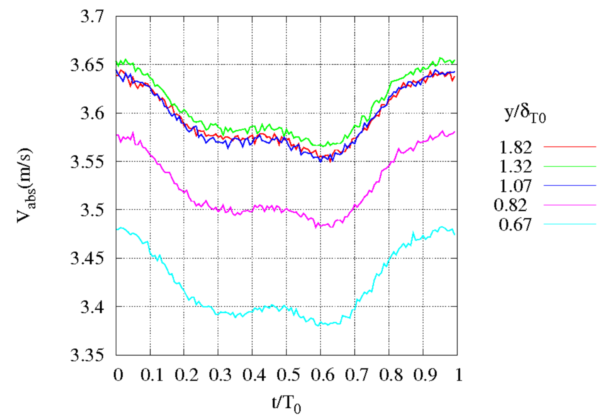

FIGURE 11. Velocity distribution on the pressure side during a moving bar period

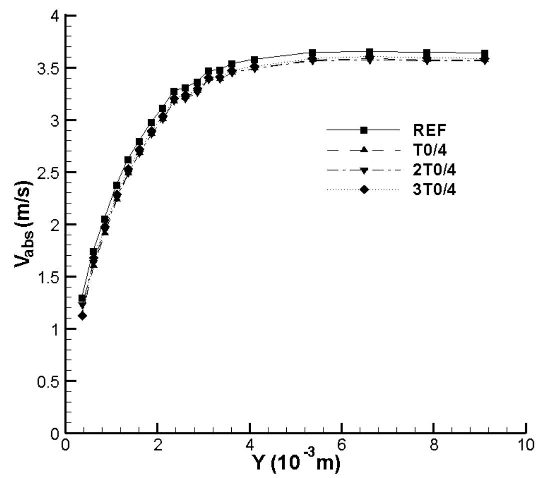

FIGURE 12. Dimensional velocity profiles - pressure side

time t	$0(REF)$	$T_0/4$	$2T_0/4$	$3T_0/4$
δ (mm)	5.00	5.08	5.12	5.22
V_{ext} (m/s)	3.64	3.58	3.75	3.75
δ_1(mm)	1.02	1.09	1.07	1.04
δ_2 (mm)	0.52	0.54	0.54	0.52
H_{12}	1.96	2.00	1.97	2.02

TABLE 2. Integral quantities - pressure side

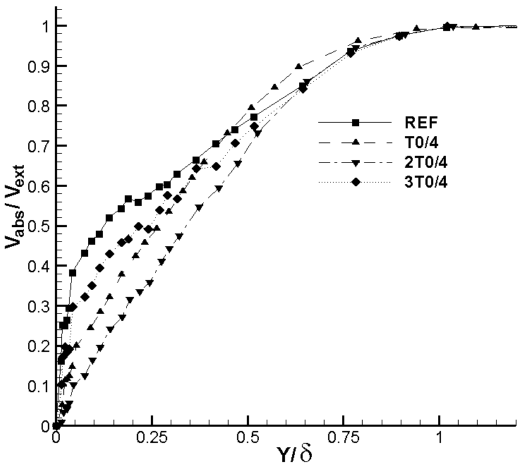

FIGURE 13. Dimensionless velocity profiles - suction side

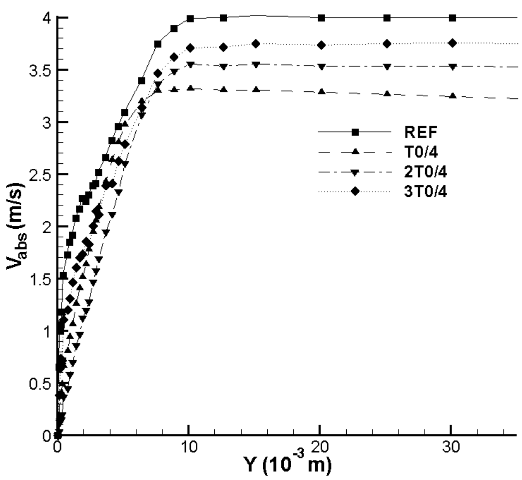

FIGURE 14. Dimensional velocity profiles - suction side

time t	$0(REF)$	$T_0/4$	$2T_0/4$	$3T_0/4$
δ	9.92	8.11	9.75	9.92
$V_{ext}(m/s)$	4.00	3.32	3.56	3.72
δ_1	2.63	2.45	3.55	2.91
δ_2	1.52	1.09	1.36	1.53
H_{12}	1.73	2.25	2.61	1.90

TABLE 3. Integral quantities - suction side

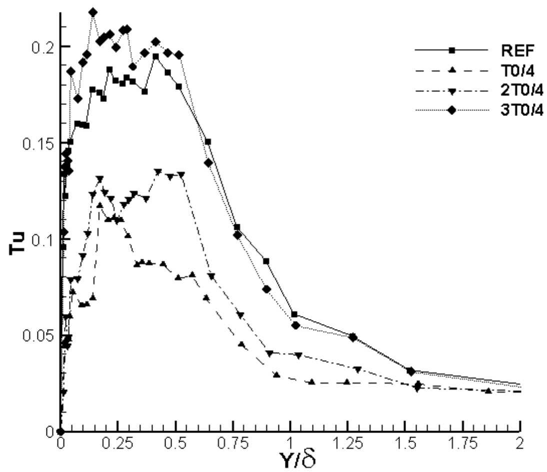

FIGURE 15. Turbulence level T_u - suction side

CONCLUSION

The potential effect has not been widely studied in the past. The decrease of the spacing between rotating and non rotating components of turbomachines due to the reduction in length of engines induces an increase of the potential and viscous effects in modern turbomachinery.

An experimental and numerical study of a rotor-stator flow field has been performed. A model of a turbomachine including an inlet guide vane followed by a rotating row of bars, itself followed by flaps, is chosen. This arrangement, far from that of a real turbine, is a very simple approximation of a turbomachine. We believe that a simple experiment where phenomena have been separated may help the understanding of flow physics and therefore may help the real world turbines (regarding unsteady heat transfer, unsteady wake generation and noise prediction for example). The Reynolds number is typical of a low pressure turbine stage. The velocities in the experimental set up are very low, a preconditioning method is applied for the Navier Stokes computation.

The numerical investigation has shown the complexity of the flow. A rotating row has an important effect on the flow on both upstream and downstream rows. Wake and boundary layers of the upstream row are modulated by the potential interaction. A periodic evolution of the pressure, entropy and velocity is found from the velocity peak on the suction side to the trailing edge. The flow on the vane pressure side is also disturbed.

The large-scale turbine blade used has sufficiently thick boundary layers to permit near wall measurements. The boundary layer at the end of the suction side is roughly 10 mm thick. The fluctuations on the pressure side due to the rod motion are weak (1%) and lower than predicted by the numerical study. On the suction side, the fluctuations are stronger (20%), an unsteady boundary layer at the trailing edge is shown, in good agreement with the numerical estimation.

This is a first approach of the study on a simple geometry. For other configurations such as turbine impulse blades or compressor blades, the impact of the modulation of the upstream flow by a downstream rotating row could be more important and separation on the blade may occur.

ACKNOWLEDGMENT

Thanks to C. Deslot for her previous work on the potential field on our configuration, and her kind help.

REFERENCES

[1] Korakianitis, T., 1992. "On the prediction of unsteady forces on gas turbine blades. ii: analysis of the results". *Journal of Turbomachinery,* ***114***(1), pp. 123–131.

[2] Korakianitis, T., 1992. "Blade-loading effects on the propagation of unsteady flow and on forcing functions in axial-turbine cascades". *J.Phys.III France,* ***2***, pp. 507–525.

[3] Parker, R., 1970. "Relation between blade row spacing and potential flow interaction effects in turbo-machines". In Proceedings of the Institution of Mechanical Engineers (London), Vol. 184, pp. 110–111.

[4] Opoka, M. M., Thomas, R. L., and Hodson, H. P., 2008. "Boundary layer transition on the high lift t106a low-pressure turbine blade with an oscillating downstream pressure field". *Journal of Turbomachinery,* ***130***, p. 021009.

[5] Hsu, S. T., and Wo, A. M., 1998. "Reduction of unsteady blade loading by beneficial use of vortical and potential disturbances in an axial compressor with rotor clocking". *Journal of Turbomachinery,* ***120***, p. 705.

[6] Dring, R. P., Joslyn, H. D., Hardin, L. W., and Wagner, J. H., 1982. "Turbine rotor-stator interaction". *ASME Journal of Engineering for Power,* ***104***(3), pp. 729–742.

[7] Parker, R., 1967. "Calculation of flow through cascades of blades having relative motion and the generation of alterning pressures and forces due to interaction effects". *Proceedings of the Institution of Mechanical Engineers,* ***182***, pp. 229–242.

[8] Parker, R., and Watson, J. F., 1972. "Interaction effects between blade rows in turbomachines". *Proceedings of the Institution of Mechanical Engineers,* ***186***.

[9] Korakianitis, T., 1993. "On the propagation of viscous wakes and potential flow in axial-turbine cascades". *Journal of turbomachinery,* ***115***(1), pp. 118–127.

[10] Deslot, C., 2009. "Les interactions rotor-stator en turbine : l'effet potentiel remontant". PhD thesis, École Centrale de Lyon.

[11] Smith, B., 1995. "Prediction of hypersonic shock wave turbulent boundary layer interactions with the k-l two equation turbulence model". In AIAA, Aerospace Sciences Meeting and Exhibit, 33 rd, Reno, NV.

[12] Deslot, C., Kulisa, P., and Bario, F., 2009. "Simulation of potential rotor-stator interaction in an axial turbine with downstream moving cylinders". *Proceeding of the 8th European Turbomachinery Conference*.

[13] Kulisa, P., and Dano, C., 2006. "Assessment of linear and non-linear two-equation turbulence models for aerothermal turbomachinery flows". *Journal of Thermal Science,* ***15***(1), pp. 14–26.

[14] Cambier, L., and Veuillot, J., 2008. "Status of the elsA CFD software for flow simulation and multidisciplinary applications". In Forty-sixth AIAA Aerospace Sciences Meeting and Exhibit, AIAA-2008, Vol. 664.

[15] Jameson, A., and Baker, T., 1987. "Improvements to the aircraft Euler method". In AIAA, Aerospace Sciences Meeting, 25 th, Reno, NV, p. 1987.

[16] Weiss, J., and Smith, W., 1995. "Preconditioning applied to variable and constant density flows". *AIAA journal,* ***33***(11), pp. 2050–2057.

[17] Choi, Y., and Merkle, C., 1993. "The application of preconditioning in viscous flows". *Journal of Computational Physics,* ***105***(2), pp. 207–223.

[18] Chorin, A., 1967. "A numerical method for solving incompressible viscous flow problems". *Journal of Computational Physics,* ***2***(1), pp. 12–26.

[19] Turkel, E., Vasta, V., and Radespiel, R., 1996. "Preconditioning Methods for Low-Speed Flows.". *AIAA paper*.

[20] Arnal, D., Habiballah, M., and Coustols, E., 1984. "Théorie de l'instabilité laminaire et critères de transition en écoulement bi et tridimensionnel= Laminar instability theory and transition criteria in two-and three-dimensional flow". *La Recherche Aérospatiale*(2), pp. 125–143.

[21] Bario, F., and Beral, C., 1998. "Boundary layer measurements on the pressure and suction sides of a turbine inlet guide vane". *Experimental Thermal and Fluid Science,* ***17***(1-2), pp. 1–9.